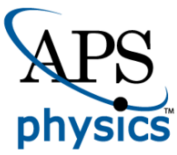

Synthesizing arbitrary lattice models using a single degenerate cavity

Su Wang, Xiang-Fa Zhou, Guang-Can Guo, Han Pu, and Zheng-Wei Zhou

Phys. Rev. A **100**, 043817 — Published 11 October 2019

DOI: 10.1103/PhysRevA.100.043817

Synthesizing arbitrary lattice models using a single degenerate cavity

Su Wang[1,2], Xiang-Fa Zhou[1,2,*] Guang-Can Guo[1,2], Han Pu[3,†] and Zheng-Wei Zhou[1,2,‡]
[1]*Key Laboratory of Quantum Information, Chinese Academy of Sciences, University of Science and Technology of China, Hefei, 230026, China*
[2]*Synergetic Innovation Center of Quantum Information and Quantum Physics, University of Science and Technology of China, Hefei, 230026, China*
[3]*Department of Physics and Astronomy, and Rice Center for Quantum Materials, Rice University, Houston, TX 77251, USA*

We propose a general method to simulate arbitrary lattice models using a single degenerate cavity. Such a cavity supports a large number of degenerate optical modes with different angular momenta. Couplings between different optical modes can be readily controlled. These features allow us to simulate lattice models that are not convenient to realize using other systems, particularly models in high dimensions and with complicated hopping amplitudes. As a concrete example, we demonstrate how to construct two topological lattice models: the two-dimensional Haldane model and a four-dimensional time-reversal invariant model. For the latter case, we show how topological properties can be detected from the outputs of the cavity, where the 2nd Chern number can be extracted. In the presence of open boundaries, the chirality of the Weyl edge modes can also be detected using the input-output formalism of the cavity modes.

Simulating synthetic dimensions using different systems presents an important frontier in quantum simulation and has received great attention in recent years [1–23]. Physically, synthetic dimensions not only enable us to simulate various novel physics in a simple and economic way, it also provides the opportunity of exploring new physics that cannot be implemented in conventional materials, such as topologically non-trivial high dimensional systems [5, 8, 12, 13, 23], synthetic metamaterials [8, 10, 20, 22], etc. Currently, various degrees of freedom have been considered to act as synthetic dimensions. This includes the atomic internal states [1, 2, 5], the motional degrees of freedom for atoms in harmonic oscillators [11], the collective superradiant states of atomic ensembles [14, 15], etc [7, 9, 23].

For photonic systems, synthetic dimensions can be implemented using the photonic orbital angular momentum (OAM) degrees of freedom [16–22], or the photonic frequency comb with equal-distant level splittings [7, 9, 23]. Constructing photonic synthetic dimensions based on photonic OAM degrees of freedom was first proposed in [16] and discussed in more depth in Ref. [17–22], where a cavity system supporting a large number of degenerate photonic modes with different angular momentum is constructed. The abundance of the OAM degrees of freedom becomes a sufficient resource that allows us to simulate various novel topological physics in high-dimensional systems in a very compact manner [16]. The degeneracy of these cavity modes enables the coupling of different OAM modes using only linear optical elements. For instance, the coupling of different optical OAM modes can be realized with the aid of spatial light modulators (SLMs). Moreover, the presence of Dove-prisms can result in OAM-dependent phase shift which enables the implementing of gauge fields in the synthetic dimensions. This flexibility also opens up the possibility of implementing topological physics with tunable boundaries even when only a single cavity is employed [17].

Currently, the construction of lattice models using synthetic dimensions has been widely considered in different physical systems. From the theoretical point of view, it is desirable to explore the ultimate potential of these synthetic systems. One natural question is: Is it possible to construct general lattice models in current experimentally available systems? The positive answer of this question will not only greatly extend the application potential of synthetic dimensions in current setups, but also provides ideal platform to emulate various functional structures and devices in a compact and economic way.

In this paper, we show that the proposed degenerate cavity system have the potential to implement an arbitrary lattice model within a single degenerate cavity due to its high flexibility. This is due to the following two key reasons. First, the tremendous degeneracy of the cavity modes enable us to represent all internal and external degrees of freedom (DOF) of the lattice model using the OAM modes of photons; second, arbitrary long-range hopping can be easily implemented with SLMs inside the auxiliary cavities. We prove that based on these two key points, arbitrary lattice hopping amplitudes with complex unit cell can be constructed. As a result, arbitrary lattice models can be implemented in principle using only one degenerate cavity with finite number of auxiliary cavities. Moreover, Such a kind of quantum simulator based on single degenerate cavity has its own unique advantages. Since the lattice in the synthetic dimension is contained in a zero-dimensional physical system, this allows us to easily detect various physical characteristics of high-dimensional systems by using input-output relation in quantum optics. To illustrate this advantage, we show that the system can sim-

* xfzhou@ustc.edu.cn
† hpu@rice.edu
‡ zwzhou@ustc.edu.cn

ulate the four dimensional (4D) extension of the quantum anomalous Hall effect, where the 2nd Chern number and Weyl chiral edge states can be detected from the input-output formalism of the cavity system. This model, with its complicated hopping amplitude, is very difficult to simulate using other systems. Its realization using degeneracy cavity as we illustrate here represents a clear demonstration of its flexibility. Our work thus sets up a promising way of exploring quantum topological physics using a single degenerate cavity.

I. ARBITRARY LATTICES FOR ARTIFICIAL DIMENSIONAL SYSTEM

The explicit construction of the degenerate cavity system can be found elsewhere [16, 17, 20]. Our construction scheme is based on the following observations. First, the cavity supports a large number of degenerate optical modes characterized with different OAMs. Practically, the degeneracy is only limited by the size of the cavity mirrors, which can then be appropriately adjusted to satisfy our requirement. Second, different cavity modes can be coupled using ancillary cavities assisted with SLMs. In principle, these ancillary circuits can be added into the cavity as we need. Finally, coupling between different OAM modes can be implemented using Dove-prisms, where an OAM-dependent phase shift allow us to construct all possible hopping elements.

Based on the above outline, we now introduce the basic components to realize arbitrary lattice models in artificial dimensional system, as shown in Fig. 1. The main ideas can be summarized as follows. First, thanks to the tremendous degeneracy of the photonic modes in the cavity, we can number all the internal and external DOF for the lattices model and map them to the OAM modes of the cavity. Second, hoppings between different sites in the lattice model now corresponds to couplings between OAM cavity modes, which can be implemented using auxiliary cavities with the help of SLMs. Since the hopping range can be controlled by the hopping steps of SLMs, This also enable us to realize high-dimensional lattice models by introducing long-range hopping terms. Thirdly, for lattice models with complex internal structure within each unit cell, the hopping amplitudes usually becomes site-dependent. In this case, a general *hopping-amplitude-controlling* procedure is necessary to synthesize the desired lattice model. As we will show below, this is always possible in our system by employing finite auxiliary optical circuits.

We consider a general lattice model in d spatial dimension. Let N_μ ($\mu = 1, 2, ..., d$) denote the number of sites in the i^{th} dimension. In addition, each site hosts N_0 internal states. We define a vector $\vec{N} \equiv (N_0, N_1, N_2, \ldots, N_d)$ to characterize this system. A particular state of the lattice model can be denoted by the vector $\vec{l} = (l_0, l_1, l_2, \ldots, l_d)$ with $l_0 \in (0, 1, \ldots, N_0 - 1)$ marking

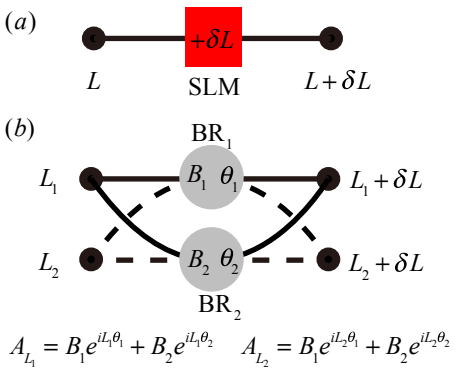

FIG. 1. The basic components to realize the arbitrary lattice using the artificial degrees of freedom (DOF) with a concrete example in Fig. 2. The basic components contain three steps including one-dimensionalization, hopping terms mapping, and hopping amplitudes controlling. One-dimensionalization is just marking each DOF in lattice system with an integer corresponding with that in artificial system. (a) The components of hopping terms mapping. Hopping terms mapping is to create hopping terms between the artificial DOF, which corresponding with the lattice system DOF, using spatial light modulators (SLMs). The SLM induces hopping terms between the light with orbital angular momentum (OAM) L and $L + \delta L$. (b) The components of hopping amplitudes controlling. Hopping amplitudes controlling process is to realize arbitrary hopping amplitudes, where beam rotators (BRs) induce OAM dependent hopping amplitudes. The BR_1 and BR_2 induce $B_1 \exp(iL\theta_1)$ and $B_2 \exp(iL\theta_2)$ hopping amplitudes for OAM mode L, respectively. The hopping amplitude for OAM mode L_1 (L_2) is A_{L_1} (A_{L_2}), respectively, which can be controlled by modifying B_1 and B_2, arbitrarily.

the internal state and $l_\mu \in (0, 1, \ldots, N_\mu - 1)$ labeling the site in the d-dim space. Thus in the cavity system, each lattice site can then be mapped to the OAM mode with $L = (\vec{l})^T \cdot \vec{C}$, where $\vec{C} = (C_0, C_1, \ldots, C_d)$ with $C_0 = 1$ and $C_\mu = \Pi_{\nu=0}^{\mu-1} N_\nu$ the total number of DOF along all the ν-th dimensions with $\nu < \mu$.

The hopping terms in the lattice model with hopping step $\delta\vec{l} = (\delta l_0, \delta l_1, \delta l_2, \ldots, \delta l_d)$ corresponds the coupling between two cavity modes whose OAMs differing by the amount

$$\delta L = (\delta\vec{l})^T \cdot \vec{C}. \tag{1}$$

Such a coupling can be implemented using one auxiliary circuit by inserting two SLMs with hopping steps $\pm\delta L$, respectively. Finally, the on-site energy shift terms can be realized in the same manner with $\delta L = 0$. After these process, we have succeed in mapping the lattice hopping terms

$$\hat{H}_{\delta\vec{l}} = \sum_{\vec{l}} B_{\delta\vec{l}} \hat{a}^\dagger_{\vec{l}+\delta\vec{l}} \hat{a}_{\vec{l}} + \text{h.c.}, \tag{2}$$

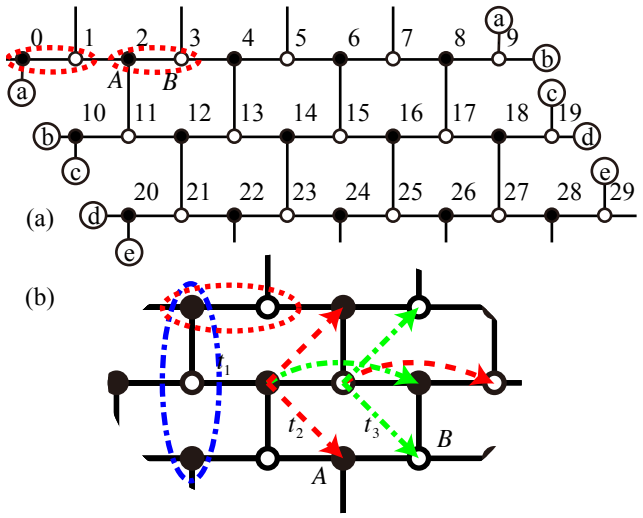

FIG. 2. (a) The brick lattice structure with the nearest hopping terms and next nearest hopping terms (not show), realized by the OAM synthetic system. The brick lattice contains two types internal states, including solid dot A and hollow dot B, for each unit site, which is marked by the red dash circle. For this case, we choose the number of unit site in the first dimension $N_1 = 5$, so the lattice contains ten states in the first line. The circles $a - e$ are the long-distance hopping terms on the edge induced by the hopping terms in the OAM system. (b) All hopping terms of Haldane model (brick lattice). The system contains nearest hopping terms, marking by the black solid lines t_1, and next nearest hopping terms $t_2 = t\exp(i\phi)$ and $t_3 = t\exp(-i\phi)$, marking by red dash lines and green dash-dot lines, respectively. Blue dash-dot circle is the hopping terms with hopping step $\delta L = 9$.

to coupling of cavity OAM modes

$$\hat{H}_{\delta L} = \sum_{L} B_{\delta L}\hat{c}^{\dagger}_{L+\delta L}\hat{c}_{L} + \text{h.c.}, \tag{3}$$

where $\hat{a}_{\vec{l}}$ ($\hat{a}^{\dagger}_{\vec{l}}$) is the annihilation (creation) operator at $\vec{l}$ in the lattice model, and $\hat{c}_L$ ($\hat{c}^{\dagger}_L$) is the annihilation (creation) operator with OAM L in the cavity system, $B_{\delta\vec{l}}$ ($B_{\delta L}$) is the hopping amplitude of lattice model (artificial, i.e., cavity, system), respectively.

To make it more clear, we consider Haldane's model [24], which is a 2D lattice model, as an example to illustrate our construction scheme. The Hamiltonian can be written as

$$\hat{H} = t_1\sum_{\langle i,j\rangle}\hat{a}^{\dagger}_i\hat{a}_j + t\sum_{\langle\langle i,j\rangle\rangle} e^{-iv_{ij}\phi}\hat{a}^{\dagger}_i\hat{a}_j + h.c. + M\sum_i \epsilon_i\hat{a}^{\dagger}_i\hat{a}_i, \tag{4}$$

where $\langle i, j\rangle$ is the link between nearest neighbors (black solid line in Fig. 2(b)), $\langle\langle i, j\rangle\rangle$ that between next nearest neighbors (red dashed lines and green dash-dot lines in Fig. 2(b)). The whole system can be divided into two sublattices denoted with A (solid dots) and B (hollow dots), and ϵ_i equal $+1$ (-1) for A (B) sites, and v_{ij} equals -1 $(+1)$ for red dashed (green dash-dot) lines.

TABLE I. The hopping amplitudes of Haldane's model in the vector $\vec{l}$ representation

$\delta\vec{l}$	δL	$A_{\delta\vec{l},0}$	$A_{\delta\vec{l},1}$
$(0,0,0)$	0	M	$-M$
$(1,0,0),(1,-1,0),(1,-1,1)$	$1,-1,9$	t_1	0
$(0,1,0),(0,-1,1),(0,0,-1)$	$2,8,-10$	$te^{-i\phi}$	$te^{i\phi}$

In our scheme, the lattice sites in Haldane's model can be described by the vector $\vec{l} = (l_0, l_1, l_2)$ with $N_0 = 2$ representing the two sublattices A and B within each lattice site denoted by (l_1, l_2). The hopping steps $\delta\vec{l}$ contain seven different types, and the Hamiltonian can then be rewritten as

$$\hat{H} = \sum_{\vec{l},\delta\vec{l},l_0} A_{\delta\vec{l},l_0}\hat{a}^{\dagger}_{\vec{l}+\delta\vec{l}}\hat{a}_{\vec{l}} + h.c., \tag{5}$$

where $A_{\delta\vec{l},l_0}$ is summarized in Tab. I and $A_{-\delta\vec{l},l_0+\delta l_0} = A^{*}_{\delta\vec{l},l_0}$. To be concrete, we choose the number of unit cell in the first dimension to be $N_1 = 5$, as shown in Fig. 2(a), where the corresponding DOF of OAM modes L are also given. Based on Eq. (1) and Tab. I, we conclude that we need six types of hopping steps to realize Haldane's model, where $|\delta L| = 0, 1, 2, 8, 9, 10$.

We also note that for high-dimensional systems, the periodic boundary condition is difficult to implement, as the translation-invariant short-range hopping terms do not vanish at the artificial boundaries after mapping to the cavity system. This will induce long-distance hopping in the original lattice system, and creates twisted boundary condition on all the dimensions except for the last one. For instance, as shown in Fig. 2(a), the short-range hopping between $L = 9$ and $L = 10$ ($L = 19$ and $L = 20$) in the synthetic system becomes a long-range one after mapping back to the original lattice model. We stress that, such twist boundaries only induce a slight shift of the energy spectrum in the momentum space, while the bulk topological properties are not changed, as shown in Appendix E.

For translation-invariant lattice model with N_0 internal states, each type of hopping with fixed steps δL can possess N_0 different hopping amplitudes at most. Therefore, we need N_0 optical circuits to realize these hoppings. As those optical circuits are all connected in the main cavity and has the same hopping step, they can interference to give a total amplitude $\sum_{j=0}^{N_0-1} B_{\delta L,j}$, where $B_{\delta L,j}$ is the hopping amplitude for the j-th optical circuit. To realize site-dependent hopping terms, we use beam rotators to induce an OAM-dependent phase shift $\exp\left(iL\theta_j\right)$ with $\theta_j = 2\pi j/N_0$. This can be realized by inserting two Dove-prisms in the auxiliary circuits, as shown in Appendix F. Using this method, the hopping amplitudes in the synthetic lattices are periodic for every N_0 OAM modes. The resulting hopping amplitudes

TABLE II. The hopping amplitudes and the number of auxiliary cavities

δL	$B_{\delta L,0}$	$B_{\delta L,1}$	# of auxiliary cavities
0	0	M	1
1	t_1	0	1
2	$t\cos\phi$	$-it\sin\phi$	2
8	$t\cos\phi$	$it\sin\phi$	2
9	$\frac{1}{2}t_1$	$\frac{1}{2}t_1$	2
10	$t\cos\phi$	$it\sin\phi$	2

can then be described by

$$A_{\delta L,l_0} = \sum_{j=0}^{N_0-1} M_{l_0,j}B_{\delta L,j} = \sum_{j=0}^{N_0-1} \exp\left(iL\theta_j\right) B_{\delta L,j}$$
$$= \sum_{j=0}^{N_0-1} \exp\left(i\frac{2\pi l_0 j}{N_0}\right) B_{\delta L,j}. \quad (6)$$

Since $M_{l_0,j}$ is invertible $N_0 \times N_0$ matrix, we can always find the appropriate $B_{\delta L,j}$ for any given hopping amplitudes $A_{\delta L,l_0}$. This indicates that for a general lattice model, all site-dependent hopping elements can be well implemented using auxiliary cavities in the degenerate cavity system.

For instance, the hopping step with $\delta L = 9$ of Haldane's model, as shown by the blue dash-dot oval in Fig. 2(b), contains two different hopping amplitudes $A_{(1,-1,1),0} = t_1$ and $A_{(-1,0,1),1} = 0$ for different internal states $j = 0$ and $j = 1$ respectively. These hoppings can be realized by the auxiliary cavities shown in Fig. 3, which contains the main cavity and two auxiliary cavities. The main cavity hold all the DOF of Haldane's model. The auxiliary cavities realize the hopping amplitudes $A_{(1,-1,1),0}$ and $A_{(-1,0,1),1}$. This is achieved by adding SLMs in the circuits which changes the OAM of the cavity modes by $\delta L = \pm 9$. Additionally, the beam rotators are inserted to induce OAM-dependent phase shifts $\exp(i2\pi Lj/2)$, as shown in Appendix F [25, 26]. The resulting hopping amplitudes are then determined by

$$\begin{pmatrix} A_{(1,-1,1),0} \\ A_{(-1,0,1),1} \end{pmatrix} = \begin{pmatrix} 1 & 1 \\ 1 & -1 \end{pmatrix} \begin{pmatrix} B_{9,0} \\ B_{9,1} \end{pmatrix}. \quad (7)$$

The desired hopping amplitudes are thus realized with $B_{9,0} = B_{9,1} = t_1/2$. Fig. 3(b) shows the relevant effective photonic circuits of the OAM system. To realize all hopping steps of Haldane's model, we need ten auxiliary cavities with hopping amplitudes, as shown in Tab. II.

The properties of the artificial cavity system can be distilled from the input-output relations of the optical modes. The spectrum and wavefunctions of the model can be determined from the transmission coefficients defined as

$$T_{L,L'} = \langle L|\frac{-i\hbar\gamma}{\hbar\omega - H_0 + i\hbar\gamma/2}|L'\rangle, \quad (8)$$

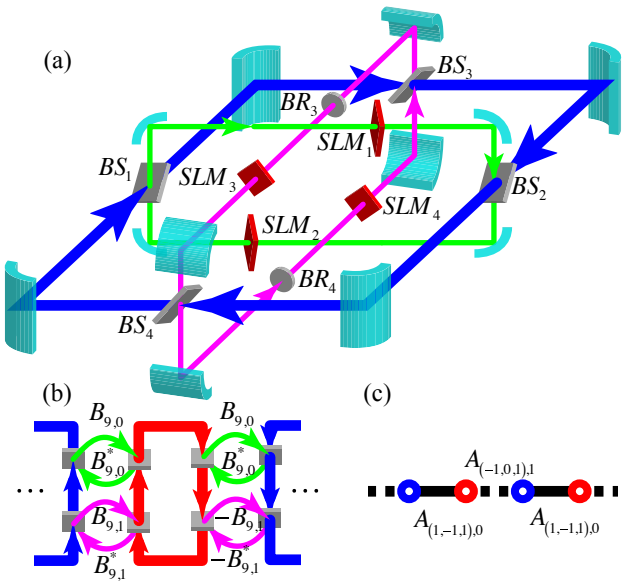

FIG. 3. The scheme for the $\delta L = 9$ hopping step for Haldane's model in orbital angular momentum (OAM) degeneracy cavities system. (a) The structure of cavities including a main cavity and two auxiliary cavities. The main cavity contains four beam splitters (BSs), which connect the main cavity and the two auxiliary cavities. Each auxiliary cavities contains a pair of spatial light modulators (SLMs) to modify the OAM of photons. After crossing SLM_1 and SLM_3 (SLM_2 and SLM_4), the photons increase (decrease) nine OAM, respectively. One of auxiliary cavity contains a pair of beam rotators (BRs), additionally. The BRs rotate the light through the propagating direction, where the photons with OAM L gain a phase $\exp(iL\theta)$, θ is the angle of rotation. The angle θ of BR_3 (BR_4) equals π ($-\pi$), respectively. (b) The effective cavity structure of $\delta L = 9$ hopping step of Haldane's model including a main cavities chain and auxiliary cavities. The main cavities chain is realized by the main cavity in (a) through the OAM DOF. The top row auxiliary cavities have the same hopping amplitude $B_{9,0}$. But the hopping amplitudes of the bottom row cavities are modified by $B_{9,1}$ and $-B_{9,1}$, periodically, as the gain of phases through BRs is periodic for OAM L. (c) The lattice structure of $\delta L = 9$ hopping step, where each unit cell contains two internal DOF. The hopping amplitudes are $A_{(1,-1,1),0} = t_1$ and $A_{(-1,0,1),1} = 0$, which is determined by Eq. (7).

where $T_{L,L'}$ is the transmission amplitude from the input mode L' to the output mode L, H_0 is the Hamiltonian to be detected, ω and γ are the effective frequency of input-output fields and homogeneous loss rate of the main cavity, respectively. For small loss rate γ and proper input-output optical modes with narrow bandwidth, the detection of the transmission coefficients allow us to determine the wavefunctions together with its topological properties, as shown in Appendix B.

Based on these discussions, we thus succeed in providing a promising route of implementing arbitrary lattice models using a degenerate cavity system with finite auxiliary optical circuits and a general method of detecting the spectrum and wavefunctions of the model.

All the hopping elements can be realized by changing the hopping steps using SLMs and gaining site-dependent phase shifts using beam rotators. We note that such beam rotator can be implemented using two Dover prisms with a rotating angle $\theta/2$ respect to each other, which can then rotate the light with an angle θ inducing a phase $\exp(iL\theta)$ to the photonic mode with OAM L.

In the following, we will construct a 4D topologically non-trivial model using the above method. We also show that even the 2nd Chern number and the chirality of the corresponded edge states can be detected in this cavity system.

II. REALIZATION OF HIGH DIMENSIONAL SYSTEM: 4D TOPOLOGICAL HAMILTONIAN

A typical 4D topology Hamiltonian with a complex unit cell $N_0 = 4$ can be written as

$$\hat{H} = \sum_{\mathbf{k}} \sum_{a=1}^{5} \hat{\psi}_{\mathbf{k}}^{\dagger} d_a(\mathbf{k}) \Gamma^a \hat{\psi}_{\mathbf{k}}, \tag{9}$$

where $\hat{\psi}_{\mathbf{k}} = (\hat{a}_{1,\mathbf{k}}, \hat{a}_{2,\mathbf{k}}, \hat{a}_{3,\mathbf{k}}, \hat{a}_{4,\mathbf{k}})^{\mathrm{T}}$ is the annihilation operator in momentum $\mathbf{k}$ with four spin components (σ in $\hat{a}_{\sigma,\mathbf{k}}$ labels the spin component). In the particular model we study here, $d_a = \sin k_a$ for $a = 1, 2, 3, 4$ and $d_5 = \left(m + \sum_{\mu=1}^{4} \cos k_\mu\right)$, and Γ^a are the 4×4 gamma matrices, which satisfy the Clifford algebra $\left\{\Gamma^a, \Gamma^b\right\} = \delta^{ab}$. The explicit forms of these gamma matrices read

$$\Gamma^1 = \sigma_3 \otimes I_2,\ \Gamma^a = \sigma_2 \otimes \tau_{a-1},\ \Gamma^5 = \sigma_1 \otimes I_2, \tag{10}$$

where $a = 2, 3, 4$, σ_{a-1} and τ_{a-1} is Pauli matrices, I_2 is the identity matrix in two dimension. This model is studied in Ref. [27] and is know to support topological phases.

The corresponding Hamiltonian in real space can be written as

$$\hat{H} = \sum_{\delta\mathbf{x}} \sum_{\mathbf{x}} \hat{\psi}_{\mathbf{x}+\delta\mathbf{x}}^{\dagger} G_{\delta\mathbf{x}} \hat{\psi}_{\mathbf{x}} + h.c. + m \sum_{\mathbf{x}} \hat{\psi}_{\mathbf{x}}^{\dagger} \Gamma^5 \hat{\psi}_{\mathbf{x}}, \tag{11}$$

where $\hat{\psi}_{\mathbf{x}} = \frac{1}{\sqrt{L^4}} \int d\mathbf{k} e^{i\mathbf{k}\cdot\mathbf{x}} \hat{\psi}_{\mathbf{k}}$ is the annihilation operator in real space, $G_{\mathbf{e}^\mu} = \Gamma^\mu/2i + \Gamma^5/2$ with $\mu = 1, 2, 3, 4$ is the hopping term along the μth direction, and $\mathbf{e}^\mu$ is the unit vector in the μth direction.

The topological properties of the system can be determined by the 2nd Chern number defined as

$$Ch_2 = \frac{1}{32\pi^2} \int d^4k \epsilon^{\mu\nu\rho\sigma} \mathrm{tr}\left[B_{\mu\nu} B_{\rho\sigma}\right], \tag{12}$$

$$B_{\mu\nu}^{\alpha\beta} = \partial_\mu A_\nu^{\alpha\beta} - \partial_\nu A_\mu^{\alpha\beta} + i\left[A_\mu, A_\nu\right]^{\alpha\beta}, \tag{13}$$

$$A_\mu^{\alpha\beta}(\mathbf{k}) = -i \langle \alpha, \mathbf{k} | \partial_\mu | \beta, \mathbf{k} \rangle, \tag{14}$$

where repeated indices are summed over, $B_{\mu\nu}$ is the Berry curvature, A_μ is the Berry connection, the indices $\mu, \nu = 1, 2, 3, 4$ label the spatial dimension, the ∂_μ is the shortcut of ∂_{k_μ}, and $|\alpha, \mathbf{k}\rangle$ is the αth eigen wavefunction at momentum $\mathbf{k}$. The model of Eq. (9) has two twice-degenerate bands with opposite Chern numbers. Topological phase transition happens when we change the mass parameter m across the critical points, where the 2nd Chern number of the low-energy band changes as follows

$$Ch_2 = \begin{cases} 0 & m < -4 \\ 1 & -4 < m < -2 \\ -3 & -2 < m < 0 \\ 3 & 0 < m < 2 \\ -1 & 2 < m < 4 \\ 0 & 4 < m \end{cases}. \tag{15}$$

In the following, we will show the explicit construction of the model using the cavity system, and the detection of its Chern number and edge states in the presence of artificial open boundaries.

A. Construct the model in cavity system

We construct this model following the procedure outlined above. First, we map all the internal and external DOF in the original Hamiltonian to the OAM modes in the degenerate cavity system. The effective Hamiltonian in terms of the cavity modes can be written as

$$\hat{H} = \sum_{\mu=1}^{4} \sum_{L} \hat{\psi}_{L+N^{\mu-1}}^{\dagger} G_\mu \hat{\psi}_L + \mathrm{h.c.} + m \sum_{L} \hat{\psi}_L^{\dagger} \Gamma^5 \hat{\psi}_L, \tag{16}$$

where the number of internal states $N_0 = 4$ and the number of sites is set to be $N_\mu = N$ ($\mu = 1, 2, 3, 4$) in each dimension for simplicity; $\hat{\psi}_L = (\hat{c}_{4L}, \hat{c}_{4L+1}, \hat{c}_{4L+2}, \hat{c}_{4L+3})^T$ with $\hat{c}_L$ ($\hat{c}_L^\dagger$) the annihilation (creation) operator on OAM L, respectively, $G_\mu = \Gamma^\mu/2i + \Gamma^5/2$ ($\mu = 1, 2, 3, 4$).

Secondly, we use the auxiliary cavities with SLMs to create all types of hopping terms, characterized by different steps in OAM coupling. For instance, each term $\hat{\psi}_{L+N^{\mu-1}}^{\dagger} G_\mu \hat{\psi}_L$ contains at most seven types hopping elements with the OAM increasing $4N^{\mu-1} + \delta l_0$ ($\delta l_0 = -3 \ldots 3$). As we have 5 terms in the Hamiltonian, we can roughly count the number of all types of hopping terms as 35. After considering the zero elements in G_μ and the possible double counting of the some hopping elements sharing the same OAM modification, the number of total auxiliary cavities can be reduced. For example, hopping elements with $\delta l_0 = -1$ in $\hat{\psi}_{L+1}^{\dagger} G_1 \psi_L$ term has the same OAM modification $\delta L = 3$ with those terms $\delta l_0 = 3$ in $\hat{\psi}_L^{\dagger} \Gamma^5 \hat{\psi}_L$, which can then be group together to improve the efficiency of the circuits.

Finally, we use the interference between the auxiliary cavities with BRs to realize the site-dependent hopping amplitudes within each complex unit cell. For each type

of the hopping term with the same hopping step δL, $\sum_{L,l_0} A_{\delta L,l_0} \hat{c}^\dagger_{4L+l_0+\delta L} \hat{c}_{4L+l_0} + h.c.$ contains four hopping amplitudes, which are $A_{\delta L,l_0}$ with $l_0 = 0,1,2,3$. This can be implemented using at most 4 auxiliary cavities with bare hopping amplitudes $B_{\delta L,j}$ $(j = 0,1,2,3)$, respectively. Each auxiliary cavity is inserted with different BRs $(\theta = 0, \pi/2, \pi, 3\pi/2)$ to realize those hopping amplitudes based on the equation

$$\begin{pmatrix} A_{\delta L,0} \\ A_{\delta L,1} \\ A_{\delta L,2} \\ A_{\delta L,3} \end{pmatrix} = \begin{pmatrix} 1 & 1 & 1 & 1 \\ 1 & i & -1 & -i \\ 1 & -1 & 1 & -1 \\ 1 & -i & -1 & i \end{pmatrix} \begin{pmatrix} B_{\delta L,0} \\ B_{\delta L,1} \\ B_{\delta L,2} \\ B_{\delta L,3} \end{pmatrix}. \tag{17}$$

Specifically, the hopping matrices Γ^5 and $G_1 = (\sigma_3/2i + \sigma_1/2) \otimes I_2$ contains hopping elements with OAM steps $\delta L = 2,4,6$. We can get these hopping amplitudes by solving Eq. (17). After dropping all the circuits with zero hopping amplitudes $B_{\delta L,j}$, we find that only $(3,2,3)$ auxiliary cavities are needed respectively, as shown in Tab. III. Similarly, we need $22, 22, 8$ auxiliary cavities to realize the hopping terms $\hat{\psi}^\dagger_{L+N} G_2 \hat{\psi}_L$, $\hat{\psi}^\dagger_{L+N^2} G_3 \hat{\psi}_L$, and $\hat{\psi}^\dagger_{L+N^3} G_4 \hat{\psi}_L$ respectively. Thus, we need roughly 60 auxiliary cavities in total to realize the model.

Next, we will show how the 2nd Chern number can be extracted from the transmission coefficients of the cavity. In the presence of open boundaries, the chirality of the edge states can also be detected as a direct consequence of nontrivial bulk topology of the model.

B. Detecting the 2nd Chern number

To obtain the value of the 2nd Chern number, we need to find the wavefunction at every momentum point and then calculate using Eq. (12). This is certainly not practical. In fact, due to the offset boundary condition in our system, we can only obtain the values of the wavefunctions at discrete momentum points defined by Eq. (E-8) in Appendix E, through detecting the transmission coefficients using input-output formalism. In the following, we will introduce an approximate method to calculate the Berry curvature and the 2nd Chern number in discretized Brillouin zone, and the method to obtain wavefunctions using the input-output formalism.

We use the wavefunctions to approximatively calculate the Berry curvature

$$U^\mu(\mathbf{k}) = u^\dagger(\mathbf{k})\, u(\mathbf{k} + \mathbf{e}^\mu), \tag{18}$$

$$\Omega^{\mu\nu}(\mathbf{k}) = i \log \Big\{ U^\mu(\mathbf{k})\, U^\nu(\mathbf{k} + \mathbf{e}^\mu) \times U^\mu(\mathbf{k} + \mathbf{e}^\nu)^{-1}\, U^\nu(\mathbf{k})^{-1} \Big\}, \tag{19}$$

where $u(\mathbf{k})$ is the wavefunction space including n_{deg} degenerate wavefunctions, $U^\mu(\mathbf{k})$ is the link variable, $\Omega^{\mu\nu}(\mathbf{k})$ is the field strength [28], each of $U^\mu(\mathbf{k})$ and $\Omega^{\mu\nu}(\mathbf{k})$ is a $n_{\text{deg}} \times n_{\text{deg}}$ matrix. In our cases, the link variable and the field strength can be extended to those in arbitrary quadrangle discrete Brillouin zone, e.g. momentum space in Eq. (E-8) of Appendix E, where each of the field strength $\Omega^{\mu\nu}(\mathbf{k})$ can be defined by four wavefunction spaces near $\mathbf{k}$. The 2nd Chern number [5] can be approximated as

$$Ch_2 \simeq \frac{1}{4\pi^2} \sum_{\mathbf{k}} \text{Tr} \Big[\Omega^{12}(\mathbf{k})\, \Omega^{34}(\mathbf{k}) + \Omega^{41}(\mathbf{k})\, \Omega^{32}(\mathbf{k}) + \Omega^{31}(\mathbf{k})\, \Omega^{24}(\mathbf{k}) \Big], \tag{20}$$

where we have approximated the integral in Eq. (12) by a discrete summation over the first Brillouin zone. This is to anticipate that we can only obtain the values of wavefunctions at discrete momentum points. To obtain the 2nd Chern number, we need the wavefunctions in momentum space. To this end, we use the standard input-output formalism of the cavity to define the transmission coefficients as

$$T_{\sigma\mathbf{x},\sigma'\mathbf{x}'} = \langle \sigma\mathbf{x} | \frac{-i\hbar\gamma}{\hbar\omega - H_0 + i\hbar\gamma/2} | \sigma'\mathbf{x}' \rangle. \tag{21}$$

where ω is the frequency of the input fields, $H_0 = \sum_{\sigma\mathbf{x},\sigma'\mathbf{x}'} |\sigma\mathbf{x}\rangle\, H_{0,\sigma\mathbf{x},\sigma'\mathbf{x}'}\, \langle \sigma'\mathbf{x}'|$ with σ the spin label at the lattice site $\mathbf{x}$, and γ the homogeneous loss rate of the main cavity. Using the spectrum representation of the Hamiltonian in momentum space, we find that the Fourier components of $T_{\sigma\mathbf{x},\sigma'\mathbf{x}'}$ can be rewritten as

$$T_{\sigma\mathbf{0},\sigma'\mathbf{k}'}(\omega) \simeq -2 \sum_{\omega_{\mathbf{k},n}=\omega} u^*_{n,\sigma} u_{n,\sigma'}, \tag{22}$$

where we have set $\mathbf{x} = (0,0,0,0)$, and $\gamma \to 0$ such that only states with the eigen-energy $\omega_{\mathbf{k},n} = \omega$ contribute most to the summation, and $u_{n,\sigma}$ is the nth eigen-vector of the Hamiltonian $H_{\mathbf{k}}$ with spectrum $\omega_{\mathbf{k},n} = \omega$. By scanning the frequency of the input photons and the lattice index in $T_{\mathbf{x}\sigma,\mathbf{x}'\sigma'}$, we can obtain similar constraints as Eq. (22), which can then be used to determine all the linear independent wavefunctions of the original Hamiltonian. Accordingly, all the relevant topological quantities related to H_0 can be calculated.

Figure 4 shows the approximate value of 2nd Chern number Ch_2 of the twice-degenerate ground state as functions of various experimental parameters including the mass parameter m, the number of sites in each dimension N, and the cavity loss rate γ in discrete momentum space shown in Eq. (E-8) with $L_\mu = N$. As can be seen from Fig. 4(a), the 2nd Chern number exhibits the desired staircase-like pattern as m is varied. This result provides a clear signature of different topological phases.

Figure 4(b) plots the Chern number as the function of N, the number of sites in each dimension, for $m = -1$ and $\gamma = 10^{-5}$, which indicates that a larger N is always helpful to obtain the correct Chern number Ch_2. A large loss rate γ would make Eq. (22) invalid, and

TABLE III. The hopping amplitudes and the number of auxiliary cavities for 4D topological model.

δL	$B_{\delta L,0}$	$B_{\delta L,1}$	$B_{\delta L,2}$	$B_{\delta L,3}$	# of auxiliary cavities
2	$(2m+1)/4$	$(2m-1)(-1+i)/8$	0	$(2m-1)(1+i)/8$	3
4	0	$-(1+i)/4$	0	$(1-i)/4$	2
6	1/4	$(1-i)/8$	0	$(1+i)/8$	3
$4N-3$	$-1/8$	$-i/8$	1/8	$i/8$	4
$4N-2$	1/4	$(-1+i)/8$	0	$-(1+i)/8$	3
$4N-1$	$-1/8$	1/8	$-1/8$	1/8	4
$4N+1$	$-1/8$	$i/8$	1/8	$-i/8$	4
$4N+2$	1/4	$(1-i)/8$	0	$(1+i)/8$	3
$4N+3$	$-1/8$	$-1/8$	$-1/8$	$-1/8$	4
$4N^2-3$	$i/8$	$-1/8$	$-i/8$	1/8	4
$4N^2-2$	1/4	$(-1+i)/8$	0	$-(1-i)/8$	3
$4N^2-1$	$-i/8$	$i/8$	$-i/8$	$i/8$	4
$4N^2+1$	$-i/8$	$-1/8$	$i/8$	1/8	4
$4N^2+2$	1/4	$(1-i)/8$	0	$(1+i)/8$	3
$4N^2+3$	$i/8$	$i/8$	$i/8$	$i/8$	4
$4N^3-2$	1/8	$i/8$	$-1/8$	$-i/8$	4
$4N^3+2$	1/8	1/8	1/8	1/8	4

cause the unwanted derivation of Ch_2 away from the ideal values. However, our calculation indicates that such derivation is almost neglectable when $\gamma < 10^{-1}$, as shown in Fig. 4(c) for $m = -1$ and $N = 15$. We also calculated standard deviation of the Chern number Ch_2, when $B_{\delta L,j}$ is assumed to have a Gauss fluctuation as in realistic experimental situations. It shows that the Chern number is robust against such noises and the above results are not qualitatively affected.

C. Weyl chiral edge states detection

In this section, we will discuss the Weyl chiral edge states of 4D topological Hamiltonian with open boundary conditions [27]. Firstly, we introduce the basic results of Weyl chiral edge states, including the spectrum and wavefunctions of the edge Hamiltonian. Next, in the presence of open boundary along the synthetic 4th direction in the 4D system, which is explicitly discussed in Appendix G, we provide a feasible scheme to reveal the chirality of the edge states using the input-output formalism.

1. *Weyl chiral edge states*

Weyl chiral edge states appear for the 4D topological non-trivial system if an open boundary is present due to the bulk-edge correspondence. These edge states are protected by the 4D topology and robust against perturbation and disorders that do not break the bulk symmetry. In our case, the 4D Hamiltonian Eq. (11) with an open boundary in the fourth direction $x_4 = 0$ can be solved analytically. The spectrum and the wavefunctions of the edge states at boundary ($x_4 = 0$) along $x_4 < 0$

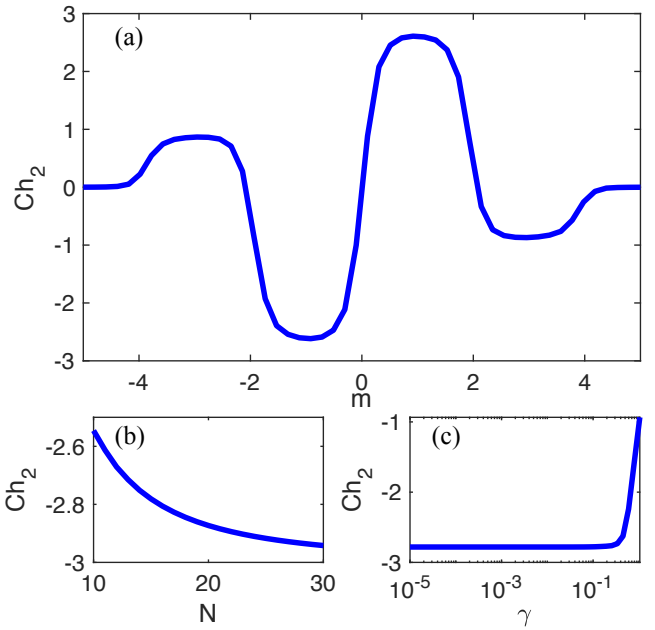

FIG. 4. The approximate 2nd Chern number varies with the mass parameter m, the number of sites in each dimension N, and the cavity loss rate γ in discrete momentum space shown in Eq. (E-8) with $L_\mu = N$. (a) the 2nd Chern number Ch_2 varies with the mass parameter m with $N = 15$ and $\gamma = 1 \times 10^{-5}$. The mass m varies from -5 to 5. (b) The Chern number varies with the number of sites in each dimension N. We set the mass $m = -1$, and $\gamma = 1 \times 10^{-5}$. (c) The Chern number varies with the loss rate γ with $m = -1$ and $N = 15$.

reads

$$E_\pm = \pm d, \tag{23}$$

$$\left|\psi_{\mathbf{k},\pm}\right\rangle = \psi_\pm\left(\vec{k}, k_4\right) \sum_{x_4 \le 0} e^{ik_4 x_4} \left|x_4\right\rangle \left|\vec{k}\right\rangle, \tag{24}$$

with

$$\psi_{\pm}\left(\vec{k},k_4\right)=\frac{1}{\sqrt{2d\left(d\mp d_1\right)}}\begin{pmatrix}0\\-id_2+d_3\\-\left(d_1\mp d\right)\\0\end{pmatrix}, \tag{25}$$

where $d=\sqrt{\sum_{\mu=1}^{3}d_\mu^2}$, and $\vec{k}$ represents the momentum in the remaining three dimensions. Since $d_5-id_4=0$ for the edge states, we have

$$k_4=i\ln\left(-m-\sum_{\mu=1}^{3}\cos k_\mu\right). \tag{26}$$

Therefore, k_4 is an imaginary number, which means that the wavefunction decays exponentially along the 4th direction when $\left|-m-\sum_{\mu=1}^{3}\cos k_\mu\right|<1$, which is typical for edge-state wavefunctions. Since $d_a(-\vec{k})=-d_a(\vec{k})$ for $a=1,2,3$, we have $\psi_+^\dagger\left(\vec{k}\right)\psi_+\left(-\vec{k}\right)=0$, which confirms the chiral property of the edge states, shown in Appendix C.

In the OAM system, artificial sharp boundaries can be implemented using beam splitters with holes, as explicitly discussed in Ref. [17] for 1D system. We note that simpler version of the idea can be generalized here to implemented open boundaries in high dimensional case, as shown in Appendix G. This allow us to detect the chirality of the edge states, which is topologically protected by the bulk gap.

2. *Detection*

In addition to calculating the Chern number of the system, topological properties can also be detected from the characteristic edge modes in the presence of open boundaries as a result of the bulk-edge correspondence. These edge states exhibit novel transportation properties protected by the bulk topology. In the following, we will propose a method to detect the chirality of the 4D edge states through the input-output formalism, which provides another simple way to illustrate the topological properties of the system.

Near a Weyl point located at $\vec{k}=\vec{k}_0$, the Hamiltonian can be linearized as

$$H\left(\vec{k}\right)=\sum_a w_a\left(\vec{k}\right)\sigma_a\simeq\sum_a\left(\vec{k}-\vec{k}_0\right)\cdot\vec{v}_a\sigma_a\,, \tag{27}$$

where $\vec{v}_a=\langle\psi_a|\,\partial H/\partial\vec{k}\,|\psi_a\rangle$ at the Weyl point, $|\psi_a\rangle$ is the eigen-vector of positive eigen-value of the Pauli matrix σ_a. The chirality of the edge state can be correspondingly defined as

$$C=\vec{v}_1\cdot\left(\vec{v}_2\times\vec{v}_3\right), \tag{28}$$

To measure the chirality, we need to link the vector $\vec{v}_a$ and the transmission coefficients defined in Eq. (8).

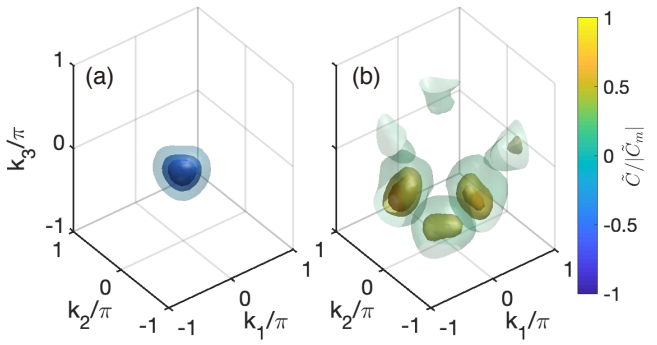

FIG. 5. The iso-surface of the detection chirality $\tilde{C}\left(\vec{k}\right)=\langle\vec{x}\rangle_1\cdot\langle\vec{x}\rangle_2\times\langle\vec{x}\rangle_3$, which is approximation of Eq. (28) using $\langle\vec{x}\rangle_a$ to replace $\vec{v}_a$, of Weyl chiral edge states with (a) the mass $m=-3$, the Chern number $Ch_2=1$ and (b) the mass $m=-1$, the Chern number $Ch_2=-3$, where $\langle\vec{x}\rangle_a$ is defined by Eq. (29) and $|\tilde{C}_m|$ is the maximum value of $|\tilde{C}|$ in momentum space $\vec{k}$, the frequency of input light is $\omega=0.5$, the loss rate is $\gamma=0.1$, the number of unit cells on each direction is $N=11$, and the width of wavepacket is $\Omega=1$.

The information of $\vec{v}_a$ can be extracted from the output fields of the cavity by detecting the average displacement of the output photons with momentum $\vec{k}_c$ as

$$\left\langle\vec{x}\left(\vec{k}_c\right)\right\rangle_a\simeq\sum_{\vec{x},\sigma}\vec{x}\left|\sum_{\vec{x}',\sigma'}T_{\sigma\vec{x}0,\sigma'\vec{x}'0}\psi^a_{\sigma'}f(\vec{x}',\vec{k}_c)\right|^2, \tag{29}$$

where $f(\vec{x}',\vec{k}_c)=\exp\left(-\vec{x}'^2/2\Omega^2+i\vec{k}_c\cdot\vec{x}'\right)$ is the distribution of the initial excitation around the center of lattice with the wavepacket width Ω and momentum $\vec{k}_c$, $\psi^a_{\sigma'}$ is the pseudo-spin state of the input fields and $\psi^a=(0,1,1,0)^T/\sqrt{2}$, $(0,1,i,0)^T/\sqrt{2}$, and $(0,1,0,0)^T$ for $a=1,2,3$, respectively. After detecting the strength of the output fields for pseudo-spin state σ at $\vec{x}$ site, $I^a_{\sigma,\vec{x}0}=\left|\sum_{\vec{x}',\sigma'}T_{\sigma\vec{x}0,\sigma'\vec{x}'0}\psi^a_{\sigma'}f(\vec{x}',\vec{k}_c)\right|^2$, we can calculate the average displacement of the output photons $\left\langle\vec{x}\left(\vec{k}_c\right)\right\rangle_a$. Here, it should be mentioned that the input pump with arbitrary modulation is unique to such kind of single degenerate cavity system, that can be easily realized by crossing holographic plate like SLM, unlike the optical delay lines in Ref. [29], which is hard to be realized by using the coherent light at different position to pump the system.

We note that the above-defined $\langle\vec{x}\rangle_a$ is proportional to the parameter $\vec{v}_a$. This is obvious if we consider the wavepacket approximation with $\vec{k}\sim\vec{k}_c+\delta\vec{k}$ near the gap close point $E_n=0$, the average displacement then reads

$$\begin{aligned}\left\langle\vec{x}\left(\vec{k}_c\right)\right\rangle_a&=i\frac{|D_1D_2|^2D_3}{\Omega^2}\langle\psi^a|\left(T^\dagger_{\vec{k}_c}\frac{\partial}{\partial\vec{k}_c}T_{\vec{k}_c}-\text{h.c.}\right)|\psi^a\rangle\\&\simeq\frac{|D_1D_2|^2D_3D_4}{\Omega^2}\langle\psi_a|\frac{\partial H}{\partial\vec{k}_c}|\psi_a\rangle\,,\end{aligned} \tag{30}$$

where $D_1 = \sum_{\vec{x}'} \exp\left(-\vec{x}'^2/2\Omega^2\right)$, $D_2 = \sum_{\delta\vec{k}} \exp\left(-\Omega^2\delta\vec{k}^2/2\right)$, $D_3 = \sum_{\vec{x}} \exp\left(-\vec{x}^2/\Omega^2\right)/x_3^2$, $D_4 = \hbar^3\gamma^3/\left(\hbar^2\omega^2 + \hbar^2\gamma^2/4\right)^2$ and $T_{\vec{k}_c} = -i\hbar\gamma/\left(\hbar\omega - H_{\vec{k}_c} + i\hbar\gamma/2\right)$. Explicit derivation of this result can be found in Appendix D. Therefore, by detecting the average displacement of the output photons, the chirality of each Weyl point can be obtained.

Fig. 5(a) (Fig. 5(b)) plots the iso-surface of the detection chirality $\tilde{C}$, which is proportional to the chirality C in Eq. (28) with $\vec{v}_a$ replaced by $\langle\vec{x}\rangle_a$, when the mass parameter $m = -3$ ($m = -1$) and Chern number $Ch_2 = 1$ ($Ch_2 = -3$), respectively. For $m = -3$, the system has one Weyl point located at $\vec{k}_c = (0, 0, 0)$, where the chirality reaches its local minimal. For $m = -1$, the system has three Weyl points located at $\vec{k}_c = (\pi, 0, 0)$, $(0, \pi, 0)$, and $(0, 0, \pi)$, respectively, where the chirality is maximal. When the Chern number equals zero, such as $m = -5$, the system does not possess Weyl points and the chirality vanishes.

III. CONCLUSIONS AND DISCUSSIONS

In summary, we have proposed a method to realize arbitrary lattice model in a single degenerate optical cavity setup. Different from previous researches [16, 18] in which the synthetic dimensions combined with the real physical dimensions are used, in the present scheme, the synthetic dimensions support the construction of the entire lattice models. Due to the highly tunability of the OAM photon, we demonstrate that we can implement all relevant hopping elements of a given lattice model after mapping all the internal and external DOF of the model to the OAM modes of cavity photons with the help of auxiliary cavities. To illustrate the validity of our approach, we provide two examples, the 2D Haldanes model and the 4D topologically nontrivial model. The latter model, in particular, is very difficult to simulate using any other systems. We propose two methods to probe the topology of the 4D system: the detection of the Chern number through transmission coefficients and the chirality of edge states using the photonic displacement around the synthetic boundaries. The present work greatly extends the ability of simulating lattice models using synthetic materials, and may provide new possibilities to design functional devices in photonic systems.

In the present system, the degeneracy of the optical modes is a crucial feature. Meanwhile, different OAM modes has its typical electric field distribution in transverse direction, and the beam size is determined by the explicit cavity parameters. Experimentally, the scalability of the scheme is closely related to our ability of implementing these beams inside the cavity. In our case, two typical size effect should be taken care of:

The first one is the beam size of the OAM modes on the cavity mirrors. Since the radius of LG modes depends on its topological charge l as $r \sim \sqrt{l}r_0$, the maximal OAM L_m allowed in the cavity is then determined by the size of cavity mirrors.Following the current experimental parameters shown in reference [19], we find that L_m can reach up to 200 or more depending on the explicit setup. This indicates that degenerate OAM modes supported in current system is large enough to simulate high-dimensional lattice models, and can be act as a testbed to verify our construction ideals.

Second, the numbers of ancillary cavities that needed for the construction of specific lattice systems, are usually model-dependent. For models with complex hopping elements, many ancillary circuits should be involved. The main cavity should be designed to have enough room for incorporating these auxiliary systems. This is possible to use a modified cavity with longer optical length D. Since a round trip of optical fields inside the cavity induces a phase $kD = 2m\pi$ with m an integer number, a longer optical length indicates a larger integer m.The free spectral range of the resonator is inversely proportional to the cavity length and reads $\Delta\nu_{FSR} = c/D$. For current setup shown in reference [19], the cavity length can be tunned from $60cm$ to $600cm$, while the FSR of the cavity can change from 500MHz to 50MHz, which is still much larger than the cavity linewidth (12MHz). This elongated cavity provides enough room for introducing different ancillary circuits into the main cavity.

After mapping into the lattice model, this degeneracy ensures lattice translation invariance. Furthermore, we can also exploit this property, by using the input-output formalism, to extract useful information about the system, such as the wave function and the associated topological characters. Moreover, in this optical synthetic system, parallel manipulation for the synthetic lattice can be achieved by only adjusting individual optical elements, which opens up the possibility of developing a special-function all-optical device [20, 22]. This can lead to new applications of topological photonics.

ACKNOWLEDGMENTS

Su Wang is indebted with Xing-Ze Qiu, Jian-Song Pan, and Wei-Feng Zhuang for invaluable discussions. This paper is funded by National Natural Science Foundation of China (Grants No. 11974334, No. 11574294, No. 61490711, and No. 11774332), National Key Research and Development Plan (Grants No. 2016YFA0301700 and No. 2016YFA0302700). HP is supported by the US NSF and the Welch Foundation (Grant No. C-1669).

APPENDIX A

In this appendix, we discuss the input-output formulation [30], which is the key to measure the Chern number and the chirality. We consider the interaction between the cavity fields and the external fields to get the

transmission properties of the cavities, which reveal the wavefunctions and spectrum of the effective Hamiltonian.

In the cavity system, the Hamiltonian of the cavity fields and external fields can be written as

$$\hat{H} = \hat{H}_0 + \hat{V}(t) + \hat{H}_{ext}, \tag{A-1}$$

where $\hat{H}_0 = \sum_{ll'} \hat{a}_l^\dagger H_{0,ll'} \hat{a}_{l'}$ is the Hamiltonian for the cavity fields,

$$\hat{V} = i\hbar \int d\omega \sum_{il} g_{il}(\omega) \left[\hat{a}_l^\dagger \hat{b}_i(\omega) - \hat{b}_i(\omega)^\dagger \hat{a}_l\right], \tag{A-2}$$

is the interaction term between the cavity fields and the external fields, $\hat{H}_{ext} = \sum_i \int d\omega \hbar\omega \hat{b}^i(\omega)^\dagger \hat{b}^i(\omega)$ is the Hamiltonian for external field, $\hat{a}_l$ ($\hat{a}_l^\dagger$) is the annihilation (creation) operator of the lth cavity field, respectively, and $\hat{b}_i$ ($\hat{b}_i^\dagger$) is that of the ith external fields, respectively. Though the Langevin equation, we can obtain the equation of motion of the cavity fields as

$$\begin{aligned}\partial_t \hat{a}_l &= -\frac{i}{\hbar}\left[\hat{a}_l, \hat{H}\right] \\ &= -\frac{i}{\hbar}\left[\hat{a}_l, \hat{H}_0\right] + g\int d\omega \hat{b}_l(\omega),\end{aligned} \tag{A-3}$$

and that of the external field

$$\partial_t \hat{b}_i = -g\hat{a}_i - i\omega \hat{b}_i(\omega), \tag{A-4}$$

where we assume $g_{il}(\omega) = g\delta_{il}$. By solving these equation, we have

$$\partial_t \hat{a}_l = -\frac{i}{\hbar}\left[\hat{a}_l, \hat{H}_0\right] + \sqrt{2\pi} g \hat{d}_{in,l}(t) - \pi g^2 \hat{a}_l(t), \tag{A-5}$$

$$\partial_t \hat{a}_l = -\frac{i}{\hbar}\left[\hat{a}_l, \hat{H}_0\right] + \sqrt{2\pi} g \hat{d}_{out,l}(t) + \pi g^2 \hat{a}_l(t), \tag{A-6}$$

where

$$\hat{d}_{in,l} \equiv -\frac{1}{\sqrt{2\pi}} \int d\omega \hat{b}_l(\omega, t_0) e^{i\omega(t_0 - t)}, \tag{A-7}$$

$$\hat{d}_{out,l} \equiv -\frac{1}{\sqrt{2\pi}} \int d\omega \hat{b}_l(\omega, t_1) e^{i\omega(t_0 - t)}, \tag{A-8}$$

t_0 (t_1) is the initial (final) time, respectively. After Fourier transformation in time, we obtain the input-output formulation

$$\hat{d}_{out}(\omega) = \left(1 - \frac{i2\pi\hbar g^2}{\hbar\omega - H_0 + i\pi\hbar g^2}\right) \hat{d}_{in}(\omega), \tag{A-9}$$

where $\hat{d}_{in,l}(t) = \int d\omega e^{-i\omega t} \hat{b}_l(\omega)$. Then the transmission coefficient is

$$T_{ll'} = \langle l | \frac{-i\hbar\gamma}{\hbar\omega - H_0 + i\hbar\gamma/2} \left| l' \right\rangle, \tag{A-10}$$

where $H_0 = \sum_{ll'} |l\rangle H_{0,ll'} \langle l'|$, l and l' label the cavity modes, and $\gamma = 2\pi g^2$ is the loss rate.

APPENDIX B

In this appendix, we will introduce the method to detect the wavefunctions through the input-output formulation, with which we can calculate the Chern number. Assume that the cavity system with low loss rate, we consider the input light with momentum k in the synthetic dimension and detect all the quasi-spin σ of the unit cell located at $x = 0$. By scanning the frequency of the input field, we can obtain the spectrum and the wavefunctions to calculate the Chern number.

The Hamiltonian of the cavity can be written as

$$H_0 = \sum_{\sigma,\sigma',x,x'} |\sigma x\rangle H_{\sigma,\sigma',x-x'} \left\langle \sigma' x' \right|, \tag{B-1}$$

where $x(x')$ is the unit cell location, $\sigma(\sigma')$ is the quasi-spin in one unit cell. The transmission coefficient in coordinate space can be written as

$$T_{\sigma x,\sigma' x'}(\omega) = \langle \sigma x | \frac{-i\hbar\gamma}{\hbar\omega - H_0 + i\hbar\gamma/2} \left| \sigma' x' \right\rangle \tag{B-2}$$

After Fourier transformation on x', we have

$$T_{\sigma x,\sigma' k'}(\omega) = e^{-ik'x} \sum_n u_{n,\sigma'}^* \frac{-i\hbar\gamma}{\hbar\omega - \hbar\omega_n + i\hbar\gamma/2} u_{n,\sigma}, \tag{B-3}$$

where $u_{n,\sigma}$ is the wavefunction at momentum k', whose energy is $\hbar\omega_n$. After setting $x = 0$, $\omega = \omega_{n'}$, $\gamma \to 0$, we find that the transmission coefficient is proportional to the eigenvector of Hamiltonian H_0 with the energy $\omega_{n'}$ as

$$T_{\sigma 0,\sigma' k'}(\omega_{n'}) \simeq -2 \sum_{\omega_n = \omega_{n'}} u_{n,\sigma}^* u_{n,\sigma'}. \tag{B-4}$$

Although the transmission coefficient is the sum of all the wavefunctions of the energy, we can obtain each wavefunction, by detecting all the quasi-spin σ to get the linear independent wavefunction space for the degeneracy Hamiltonian, as $u_{n,\sigma}^*$ is the sum coefficients of wavefunctions. The transmission coefficient is the key to detect the wavefunctions to calculate the Chern number.

APPENDIX C

In this section, we will introduce the basic results of the edge states in the 4D topological non-trivial system [27] with an open boundary condition using the method shown in the paper [31]. By introducing the ansatz wavefunctions with exponential decay on the boundary, we can obtain the Hamiltonian and chirality condition in the quasi-spin space for edge states. Subsequently we can obtain the spectrum and the corresponding chiral wavefunctions, which satisfy $\psi_\pm^\dagger\left(\vec{k}\right)\psi_\pm\left(-\vec{k}\right) = 0$, where $\psi_\pm\left(\vec{k}\right)$ is wavefunction of spin at momentum $\vec{k}$.

The bulk Hamiltonian can be written as

$$H = \sum_{\mathbf{k}} \sum_{a=1}^{5} d_a(\mathbf{k}) \Gamma^a |\mathbf{k}\rangle \langle \mathbf{k}| \tag{C-1}$$

where $d_a(\mathbf{k}) = \left(\sin k_1, \sin k_2, \sin k_3, \sin k_4, \left(m + \sum_{\mu=1}^{4} \cos k_\mu\right)\right)_a$, and Γ^a is the gamma matrix defined by Eq. (10). After Fourier transformation $|\mathbf{k}\rangle = \sum_{x_4} e^{ik_4 x_4} \left|\vec{k}, x_4\right\rangle$, we can get the Hamiltonian with an open boundary in the 4th direction

$$H = \sum_{\vec{k}} \sum_{x_4 \le 0} \left|\vec{k}, x_4\right\rangle \left(\sum_{a=1}^{3} d_a\left(\vec{k}\right) \Gamma^a + \left(m + \sum_{\mu \neq 4} \cos k_\mu\right) \Gamma^5 \right) \left\langle \vec{k}, x_4 \right| + \sum_{\vec{k}} \sum_{x_4 \le 0} \left(\left|\vec{k}, x_4 - 1\right\rangle \frac{1}{2} \left(\Gamma^5 - i\Gamma^4\right) \left\langle \vec{k}, x_4 \right| + h.c. \right). \tag{C-2}$$

The wavefunctions of edge states can be written as

$$|\psi_{\mathbf{k}}\rangle = \psi_s\left(\vec{k}, k_4\right) \sum_{x_4 \le 0} e^{ik_4 x_4} |x_4\rangle \left|\vec{k}\right\rangle. \tag{C-3}$$

From the Schrödinger's equation, we have

$$\begin{aligned} H|\psi_{\mathbf{k}}\rangle = \sum_{x_4 \le 0} \sum_{a=1}^{5} \Bigg[& d_a(\mathbf{k}) \Gamma^a \psi_s\left(\vec{k}, k_4\right) e^{ik_4 x_4} \left|\vec{k}, x_4\right\rangle \\ & -\frac{1}{2} \left(\Gamma^5 - i\Gamma^4\right) \psi_s\left(\vec{k}, k_4\right) e^{ik_4} \left|\vec{k}, 0\right\rangle \Bigg] \\ = E|\psi_{\mathbf{k}}\rangle, & \end{aligned} \tag{C-4}$$

so we get

$$\sum_{a=1}^{5} d_a(\mathbf{k}) \Gamma^a \psi_s\left(\vec{k}, k_4\right) = E \psi_s\left(\vec{k}, k_4\right), \tag{C-5}$$

$$\frac{1}{2} \left(\Gamma^5 - i\Gamma^4\right) \psi_s\left(\vec{k}, k_4\right) = 0. \tag{C-6}$$

By solving it, we can get the wavefunctions of the edge states

$$\psi_{\pm} = \frac{1}{\sqrt{2d\left(d \mp d_1\right)}} \begin{pmatrix} 0 \\ -id_2 + d_3 \\ -\left(d_1 \mp d\right) \\ 0 \end{pmatrix}, \tag{C-7}$$

and the spectrum

$$E_{\pm} = \pm d, \tag{C-8}$$

where $d = \sqrt{\sum_{a=1}^{3} d_a^2}$, $d_5 - id_4 = 0$, which means

$$k_4 = i \ln\left(-m - \sum_{\mu=1}^{3} \cos k_3\right). \tag{C-9}$$

When $\left|-m - \sum_{\mu=1}^{3} \cos k_\mu\right| < 1$, the edge states exist as $\lim_{x_4 \to -\infty} \exp(ik_4 x_4) = 0$.

The edge state is chiral, as the quasi-spin states are orthogonal the opposite momentum at the same energy by $\psi_+^\dagger\left(\vec{k}\right) \psi_+\left(-\vec{k}\right) = 0$, where

$$\psi_+\left(\pm\vec{k}\right) = \frac{1}{\sqrt{2d\left(d \mp d_1\right)}} \begin{pmatrix} 0 \\ -id_2 + d_3 \\ -\left(d_1 \mp d\right) \\ 0 \end{pmatrix}. \tag{C-10}$$

APPENDIX D

In this section, we will introduce the method to detect the chirality of Hamiltonian, including the definition of chirality of a general Hamiltonian near the Weyl point, and the connection between the definition and detection method through the average displacement. For Weyl point $\vec{k}_c$, the eigen-energy of Hamiltonian $E_n = 0$, the Hamiltonian can be expanded by

$$\begin{aligned} H\left(\vec{k}\right) &= \sum_a v_a\left(\vec{k}\right) \sigma_a \\ &\simeq \sum_a \left(v_a\left(\vec{k}_c\right) + \left(\vec{k} - \vec{k}_c\right) \cdot \frac{\partial}{\partial \vec{k}_c} v_a \right) \sigma_a \\ &\simeq \sum_a \left(\left(\vec{k} - \vec{k}_c\right) \cdot \vec{v}_a \right) \sigma_a, \end{aligned} \tag{D-1}$$

where $v_a\left(\vec{k}_c\right) = 0$ vanishes and $\vec{v}_a = \partial v_a / \partial \vec{k}_c$ is finite. Then the chirality can be written as

$$C = \vec{v}_1 \cdot \left(\vec{v}_2 \times \vec{v}_3\right), \tag{D-2}$$

where

$$\vec{v}_a = \langle\psi_a| \frac{\partial}{\partial \vec{k}} H\left(\vec{k}\right) |\psi_a\rangle , \tag{D-3}$$

$|\psi_a\rangle$ is the eigen-vector of σ_a with a positive eigen-value [32]. In the condition of Weyl point $v_a\left(\vec{k}_c\right) = 0$, the vector becomes

$$\begin{aligned}\vec{v}_a &= \sum_n \langle\psi_a| \left[\frac{\partial}{\partial \vec{k}} E_n |\varphi_n\rangle \langle\varphi_n| + E_n \frac{\partial}{\partial \vec{k}} \left(|\varphi_n\rangle \langle\varphi_n|\right)\right] |\psi_a\rangle \\ &= \sum_n \frac{\partial}{\partial \vec{k}} E_n \left|\left\langle \psi_a \middle| \varphi_n \right\rangle\right|^2 ,\end{aligned} \tag{D-4}$$

where $|\varphi_n\rangle$ is the eigenvector of the Hamiltonian. Here $\sum_n E_n \frac{\partial}{\partial \vec{k}} \left(|\varphi_n\rangle \langle\varphi_n|\right) = 0$, as we have complete relation and the energy E_n is constant in Weyl point.

Then we need to prove that the average distance can be written as

$$\langle\vec{x}\rangle_a = \frac{\hbar^3\gamma^3}{\left(\hbar^2\omega^2 + \hbar^2\gamma^2/4\right)^2} \frac{|D_1 D_2|^2 D_3}{\Omega^2} \sum_n \frac{\partial}{\partial \vec{k}_c} E_n\left(\vec{k}_c\right) |\langle\psi^a| |\varphi_n\rangle|^2 ,$$

in the Weyl point, where $D_1 = \sum_{\vec{x}'} \exp\left(-\vec{x}'^2/2\Omega^2\right)$, $D_2 = \sum_{\delta\vec{k}} \exp\left(-\Omega^2\delta\vec{k}^2/2\right)$, $D_3 = \sum_{\vec{x},\sigma} \exp\left(-\vec{x}^2/\Omega^2\right) x_1^2$.

Through Fourier transformation $T_{\sigma,\vec{x}0,\sigma',\vec{x}'0} = \sum_{\delta\vec{k}} \sum_n \exp\left[-i\left(\vec{k}_c + \delta\vec{k}\right)\cdot\left(\vec{x}' - \vec{x}\right)\right] T_{\vec{k}_c+\delta\vec{k},n}$, the output fields can be written as

$$\begin{aligned} f^{\sigma}_{\mathrm{out},a}(\vec{x}) &\equiv \sum_{\vec{x}',\sigma'} T_{\sigma,\vec{x}0,\sigma',\vec{x}'0} \psi^a_{\sigma'} f\left(\vec{x}', \vec{k}_c\right) \\ &= e^{i\vec{k}_c\cdot\vec{x}} \sum_{\vec{x}',\sigma'} \sum_{\delta\vec{k}} \sum_n e^{-i\delta\vec{k}\cdot\left(\vec{x}'-\vec{x}\right) - \frac{\vec{x}'^2}{2\Omega^2}} T^{\sigma,\sigma'}_{\vec{k}_c+\delta\vec{k},n} \psi^a_{\sigma'} \\ &= e^{i\vec{k}_c\cdot\vec{x}} \sum_{\vec{x}',\sigma'} \sum_{\delta\vec{k}} e^{i\delta\vec{k}\cdot\vec{x}'} \sum_n e^{-i\delta\vec{k}\cdot\vec{x}' - \frac{\vec{x}'^2}{2\Omega^2}} T^{\sigma,\sigma'}_{\vec{k}_c+\delta\vec{k},n} \psi^a_{\sigma'} \end{aligned} \tag{D-5}$$

where $T^{\sigma,\sigma'}_{\vec{k}_c,n} = -i\hbar\gamma/\left(\hbar\omega - E_n + i\hbar\gamma/2\right)\psi^{\sigma}_n \psi^{\sigma'*}_n$, $f\left(\vec{x}', \vec{k}_c\right) = \exp\left(-\vec{x}'^2/2\Omega^2 + i\vec{k}_c\cdot\vec{x}'\right)$ is the wavepacket with momentum $\vec{k}_c$. After integrating $\vec{x}'$ and expanding $T^{\sigma,\sigma'}_{\vec{k}_c+\delta\vec{k},n}$ near $\delta\vec{k} = 0$, the output fields become

$$\begin{aligned} f^{\sigma}_{\mathrm{out},a}(\vec{x}) &= e^{i\vec{k}_c\cdot\vec{x}} D_1 \sum_{\delta\vec{k}} \sum_n e^{-\frac{\Omega^2\delta\vec{k}^2}{2} + i\delta\vec{k}\cdot\vec{x}} T^{\sigma,\sigma'}_{\vec{k}_c+\delta\vec{k},n} \psi^a_{\sigma'} \\ &\simeq e^{i\vec{k}_c\cdot\vec{x}} D_1 e^{-\frac{\vec{x}^2}{2\Omega^2}} \sum_{\delta\vec{k}} \sum_n e^{-\frac{\Omega^2}{2}\left(\delta\vec{k} - i\frac{1}{\Omega^2}\vec{x}\right)^2} \left(T^{\sigma,\sigma'}_{\vec{k}_c,n} + \delta\vec{k}\frac{\partial}{\partial\vec{k}_c} T^{\sigma,\sigma'}_{\vec{k}_c,n}\right)\psi^a_{\sigma'}, \end{aligned}$$

where $D_1 = \sum_{\vec{x}'} \exp\left(-\vec{x}'^2/2\Omega^2\right)$. After integrating $\delta\vec{k}$, we can get

$$f^{\sigma}_{\mathrm{out},a}(\vec{x}) = e^{i\vec{k}_c\cdot\vec{x}} D_1 D_2 e^{-\frac{\vec{x}^2}{2\Omega^2}} \sum_n \left(T^{\sigma,\sigma'}_{\vec{k}_c,n} + i\frac{1}{\Omega^2}\vec{x}\cdot\frac{\partial}{\partial\vec{k}_c} T^{\sigma,\sigma'}_{\vec{k}_c,n}\right)\psi^a_{\sigma'},$$

where $D_2 = \sum_{\delta\vec{k}} \exp\left(-\Omega^2\delta\vec{k}^2/2\right)$. Then the average distance

$$\begin{aligned} \langle\vec{x}\rangle_a &= \sum_{\vec{x},\sigma} \vec{x} \left|f^{\sigma}_{\mathrm{out},a}(\vec{x})\right|^2 \\ &\simeq |D_1 D_2|^2 \sum_{\vec{x}} \vec{x} e^{-\frac{\vec{x}^2}{\Omega^2}} \langle\psi^a| \left(T^{\dagger}_{\vec{k}_c} - i\frac{1}{\Omega^2}\vec{x}\cdot\frac{\partial}{\partial\vec{k}_c} T^{\dagger}_{\vec{k}_c}\right)\left(T_{\vec{k}_c} + i\frac{1}{\Omega^2}\vec{x}\cdot\frac{\partial}{\partial\vec{k}_c} T_{\vec{k}_c}\right)|\psi^a\rangle \\ &= \frac{i\,|D_1 D_2|^2}{\Omega^2} \sum_{\vec{x}} \vec{x} e^{-\frac{\vec{x}^2}{\Omega^2}} \vec{x}\cdot\langle\psi^a| T^{\dagger}_{\vec{k}_c} \frac{\partial}{\partial\vec{k}_c} T_{\vec{k}_c} - \frac{\partial}{\partial\vec{k}_c} T^{\dagger}_{\vec{k}_c} T_{\vec{k}_c} |\psi^a\rangle \\ &= \frac{i\,|D_1 D_2|^2 D_3}{\Omega^2} \langle\psi^a| T^{\dagger}_{\vec{k}_c} \frac{\partial}{\partial\vec{k}_c} T_{\vec{k}_c} - \frac{\partial}{\partial\vec{k}_c} T^{\dagger}_{\vec{k}_c} T_{\vec{k}_c} |\psi^a\rangle \end{aligned} \tag{D-6}$$

where $D_3 = \sum_{\vec{x}} \exp\left(-\vec{x}^2/\Omega^2\right) x_1^2$. We note that all the operators and wavefunctions are in the spin space, and only the even function of x_i can survive in the integral. Here $T_{\vec{k}_c} = \sum_n (G_n + iF_n) |\varphi_n\rangle \langle\varphi_n|$, $G_n = -\hbar^2\gamma^2/[2(\hbar\omega - E_n)^2 + \hbar^2\gamma^2/2]$, $F_n = -\hbar\gamma(\hbar\omega - E_n)/[(\hbar\omega - E_n)^2 + \hbar^2\gamma^2/4]$

$$\begin{aligned} T^\dagger_{\vec{k}_c} \frac{\partial}{\partial \vec{k}_c} T_{\vec{k}_c}\Big|_{E_n=0} &= \sum_n (G_n - iF_n)\left(\frac{\partial}{\partial \vec{k}_c} G_n + i\frac{\partial}{\partial \vec{k}_c} F_n\right) |\varphi_n\rangle \langle\varphi_n| \\ &= \sum_n \left(G_n \frac{\partial}{\partial \vec{k}_c} G_n + F_n \frac{\partial}{\partial \vec{k}_c} F_n + iG_n \frac{\partial}{\partial \vec{k}_c} F_n - iF_n \frac{\partial}{\partial \vec{k}_c} G_n\right) |\varphi_n\rangle \langle\varphi_n| . \end{aligned}$$

Here we ignore the variation of the wavefunctions, because $\frac{\partial}{\partial \vec{k}_c} \sum_n |\varphi_n\rangle \langle\varphi_n| = 0$, when $E_n = 0$. Then

$$\begin{aligned} T^\dagger_{\vec{k}_c} \frac{\partial}{\partial \vec{k}_c} T_{\vec{k}_c}\Big|_{E_n=0} - \text{h.c} &= 2i \sum_n \left(G_n \frac{\partial}{\partial \vec{k}_c} F_n - F_n \frac{\partial}{\partial \vec{k}_c} G_n\right) |\varphi_n\rangle \langle\varphi_n| \\ &= 2i \sum_n \left(\begin{array}{l} \frac{\hbar^2\gamma^2/2}{\left(\hbar\omega - E_n\left(\vec{k}_c\right)\right)^2 + \hbar^2\gamma^2/4} \left(\hbar\gamma\left(\hbar\omega - E_n\left(\vec{k}_c\right)\right) \frac{\partial}{\partial \vec{k}_c} \frac{1}{\left(\hbar\omega - E_n\left(\vec{k}_c\right)\right)^2 + \hbar^2\gamma^2/4} - \frac{1}{\left(\hbar\omega - E_n\left(\vec{k}_c\right)\right)^2 + \hbar^2\gamma^2/4} \hbar\gamma \frac{\partial}{\partial \vec{k}_c} E_n\left(\vec{k}_c\right)\right) \\ \qquad - \frac{\hbar\gamma\left(\hbar\omega - E_n\left(\vec{k}_c\right)\right)}{\left(\hbar\omega - E_n\left(\vec{k}_c\right)\right)^2 + \hbar^2\gamma^2/4} \frac{\partial}{\partial \vec{k}_c} \frac{\hbar^2\gamma^2/2}{\left(\hbar\omega - E_n\left(\vec{k}_c\right)\right)^2 + \hbar^2\gamma^2/4} \end{array} \right) |\varphi_n\rangle \langle\varphi_n| \\ &= -i \frac{\hbar^3\gamma^3}{\left(\hbar^2\omega^2 + \hbar^2\gamma^2/4\right)^2} \sum_n \frac{\partial}{\partial \vec{k}_c} E_n\left(\vec{k}_c\right) |\varphi_n\rangle \langle\varphi_n| \end{aligned} \tag{D-7}$$

$$\langle \vec{x} \rangle_a = \frac{\hbar^3\gamma^3}{\left(\hbar^2\omega^2 + \hbar^2\gamma^2/4\right)^2} \frac{|D_1 D_2|^2 D_3}{\Omega^2} \sum_n \frac{\partial}{\partial \vec{k}_c} E_n \left|\left\langle \psi_a \middle| \varphi_n \right\rangle\right|^2 , \tag{D-8}$$

Comparing with

$$\vec{v}_a = \sum_n \frac{\partial}{\partial \vec{k}} E_n \left|\left\langle \psi_a \middle| \varphi_n \right\rangle\right|^2 ,$$

we know that the chirality vector is proportional to the average distance.

APPENDIX E

In this section, we will introduce the effects of the offset boundaries, which is one of the results to simulate a high dimensional system using a long distance hopping in the one-dimensional system. For simplicity, we consider a 2D system with an offset boundary along the 1st dimension and a periodic boundary along the 2nd dimension, whose Hamiltonian can be written as

$$\begin{aligned} H = &\sum_{x_1=0}^{L-2} \sum_{x_2} H_{x_1} |x_1 + 1, x_2\rangle \langle x_1, x_2| \\ &+ \sum_{x_1=0}^{L-1} \sum_{x_2} H_{x_2} |x_1, x_2 + 1\rangle \langle x_1, x_2| \\ &+ \sum_{x_2} H_{x_1} |0, x_2 + 1\rangle \langle L - 1, x_2| + h.c. \end{aligned} \tag{E-1}$$

with the offset boundary terms like $\sum_{x_2} H_{x_1} |0, x_2 + 1\rangle \langle L - 1, x_2|$. After Fourier transformation on the 2nd direction, we can get the Hamiltonian on the 1st direction with k_2 as a parameter

$$H = \sum_{k_2} H_{k_2} |k_2\rangle \langle k_2| , \tag{E-2}$$

with

$$\begin{aligned} H_{k_2} = &H_{x_1} \sum_{x_1=0}^{L-2} |x_1 + 1\rangle \langle x_1| + H_{x_2} e^{-ik_2} \sum_{x_1=0}^{L-1} |x_1\rangle \langle x_1| \\ &+ H_{x_1} e^{-ik_2} |0\rangle \langle L - 1| + h.c.. \end{aligned} \tag{E-3}$$

After setting the eigenstate of Hamiltonian H_{k_2} as

$$\left|\psi_{k_1,k_2}\right\rangle = \psi_s\left(\vec{k}\right) \sum_{x_1'} e^{ik_1 x_1'} \left|x_1'\right\rangle , \tag{E-4}$$

and solving the Schrödinger's equation, we have

$$H_{x_1 x_2} \psi_s\left(\vec{k}\right) = E_{\vec{k}} \psi_s\left(\vec{k}\right), \tag{E-5}$$

$$e^{-ik_2} e^{ik_1 L} - 1 = 0, \tag{E-6}$$

where $H_{x_1 x_2} = H_{x_1} \exp(-ik_1) + H^\dagger_{x_1} \exp(ik_1) + H_2 \exp(-ik_2) + H_2^\dagger \exp(ik_2)$. So the momentum k_1 should be

$$k_1 = \frac{2n_1\pi + k_2}{L_1}. \tag{E-7}$$

Using the similar methods, we find that the momentum in the 4D topological model should be

$$\begin{aligned} k_4 &= \frac{2\pi n_4}{L_4}, \\ k_3 &= \frac{2\pi n_3}{L_3} + \frac{2\pi n_4}{L_3 L_4}, \\ k_2 &= \frac{2\pi n_2}{L_2} + \frac{2\pi n_3}{L_2 L_3} + \frac{2\pi n_4}{L_2 L_3 L_4}, \\ k_1 &= \frac{2\pi n_1}{L_1} + \frac{2\pi n_2}{L_1 L_2} + \frac{2\pi n_3}{L_1 L_2 L_3} + \frac{2\pi n_4}{L_1 L_2 L_3 L_4}, \end{aligned} \tag{E-8}$$

where $n_\mu = 0, 1, \ldots, L_\mu - 1$, L_μ is the length on the μth direction. The offset boundary shifts the momentum slightly, which does not change the methods to detect the Chern numbers and the edge states.

APPENDIX F

In this section, we will discuss the beam rotator (BR) that induces an OAM-dependent phase shift to the cavity field, as shown in Fig. 6 [25, 26]. The BR consists of two Dove prisms, each of which transforms the photon phase $\exp(iL\varphi)$ to $\exp[iL(2\theta_1 - \varphi)]$, where θ_1 is axis angle of the Dove prism. After crossing two Dove prism with an intersecting angle $\theta/2$, the photon gains an additional phase $\exp(iL\theta)$, which induces OAM dependent hopping amplitudes.

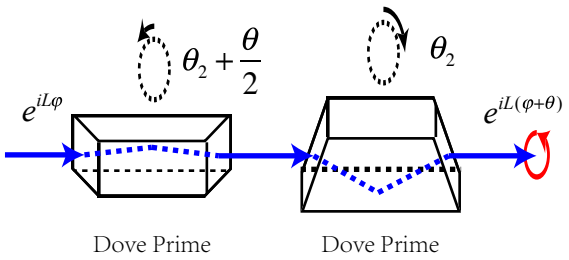

FIG. 6. Beam rotator. The beam rotator includes two Dove Primes intersect each other with an angle θ. It induces a extra phase $\exp(iL\theta)$, when a photon with orbital angular momentum (OAM) L crosses it.

APPENDIX G

In this section, we discuss the basic construction idea to implement the open boundaries along the 4th dimension in this synthetic 4D system based on a simpler version of the idea proposed in Ref. [17].

In the degenerate-cavity system, the beam size of the LG mode increases along with the OAM $|l|$. It is expected that beam spitters with holes can reflect the light, only when the light carries an OAM l that satisfies $|l| \geq L_b$. This induces a boundary at $|l| = L_b$, as shown in Fig. 7(a-b) with $L_b = 1$. Fig. 7(a) is the scheme of experimental setup to simulate 1D lattice with open boundary condition on OAM $|l| = 1$. The beam spitters (BS_1 and BS_2) with a hole block the hopping between OAM modes $l = 0$ and $l = 1$, that induces the open boundary on $l = 1$, where the effective cavities line is shown in Fig. 7(b).

The above scheme can also be generalized to construct sharp boundaries in high dimensional case. To introduce sharp boundaries along the fourth dimension discussed in the main text, the hole size in BSs should be designed such that $L_b = 4N^3$. This ensures that all hoppings $l \to l + L_b$, with $|l| < L_b$, are blocked as expected for a sharp boundary.

To estimate the sharpness of the boundaries, we calculate the reflected portion of the Laguerre-Gaussian (LG) modes on the BSs. The amplitude distribution of the vector potential of LG modes can be written as

$$\begin{aligned} u_{lp}(r, z, \phi) = {} & \frac{E_0}{w(z)} \left(\frac{\sqrt{2} r}{w(z)} \right)^{|l|} \exp\left(-\frac{r^2}{w^2(z)} \right) L_p^{|l|} \left(\frac{2r^2}{w^2(z)} \right) \\ & \times \exp\left(-ik \frac{r^2 z}{2\left(z^2 + z_R^2\right)} \right) \exp(-i\phi l) \exp(-ikz) \\ & \exp\left(i\left(|l| + 2p + 1\right) \arctan\left(\frac{z}{z_R} \right) \right), \end{aligned} \tag{G-1}$$

where r is the radial distance from the center axis of the beams, z is the axial distance from the beams' focus, ϕ is the azimuth, p is the radial index, $w = w_0 \sqrt{1 + z/z_R}$, $z_R = \pi w_0^2 / \lambda$, w_0 is the waist radius, and $L_p^{|l|}(x)$ is associated Laguerre polynomial. When the BS is located at the waist of the modes and $p = 0$, the reflected parts of the light can be written as

$$\eta_l = \frac{1}{I_0} \int_{r_h}^{\infty} r dr \int_0^{2\pi} d\phi \left| u_{l0}(r, 0, \phi) \right|^2, \tag{G-2}$$

where $I_0 = \int_0^\infty r dr \int_0^{2\pi} d\phi \left| u_{l0}(r, 0, \phi) \right|^2$, and r_h is the radius of the hole. In Fig. 7(c), we plot the intensity $rI(r) \equiv \int_0^{2\pi} d\phi r \left| u_{l0}(r, 0, \phi) \right|^2 / I_0$ of LG modes with OAM l. The maximum intensity locates at $r_0 = w_0 \sqrt{2|l| + 1}/2$, while the intensity has the same full width at half maximum (FWHM) when $l \to \infty$. After choosing r_h, we can get the effective hopping terms $\eta_l \eta_{l+m} c_{l+m}^\dagger c_l$, instead of $c_{l+m}^\dagger c_l$.

Fig. 7(d) plots the effective hopping factor η_l, where r_h is determined through the equation $\eta_{4N^3} = 1 - \eta_{4N^3+1}$ with $4N^3$ the hopping distance on the 4th-direction. In this system, the blocked hopping terms, started from $l = 0$ to $l = 4N^3$, create open boundaries along the 4th-direction in the effective 4D system. The result indicates that the boundary is very shape, sufficient for the detection of the edge states, as discussed in the main text.

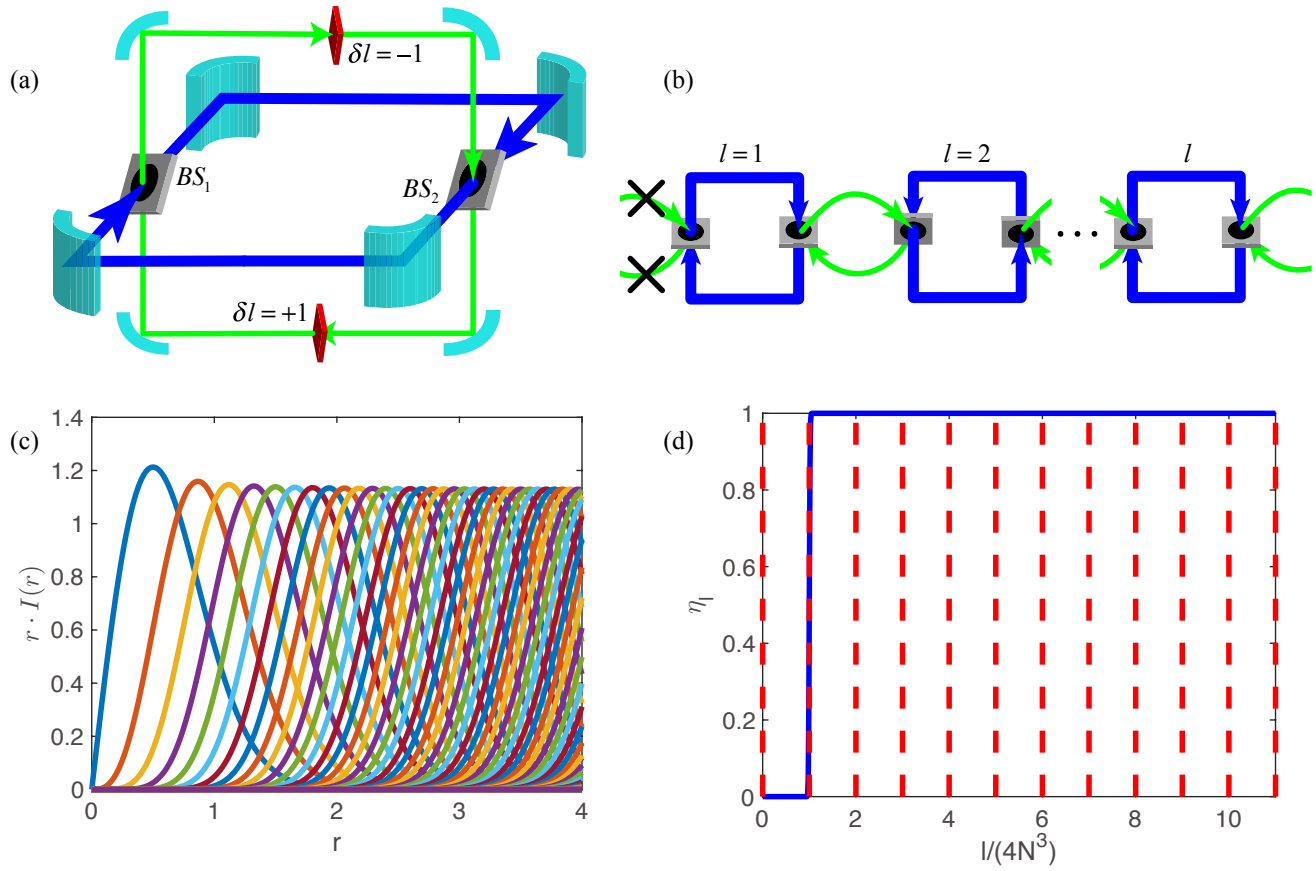

FIG. 7. (a) The scheme of experimental setup to simulate 1D lattice with open boundary condition on the left edge. The main cavity contains two beam splitters (BS_1 and BS_2) with one hole to block the hopping on the light with OAM $l = 0$. (b) The effective cavities line of (a). The holes in BSs block the hopping on the light with OAM $l = 0$. (c) The strength of light of Laguerre-Gaussian with $p = 0$ and OAM l. (d) The effective hopping factor η_l varies with the OAM l by choosing r_h to guarantee $\eta_{4N^3} = 1 - \eta_{4N^3+1}$, where the number of unit cells on one dimension $N = 11$.

[1] O. Boada, A. Celi, J. I. Latorre, and M. Lewenstein, Physical review letters **108**, 133001 (2012), https://doi.org/10.1103/PhysRevLett.108.133001.

[2] A. Celi, P. Massignan, J. Ruseckas, N. Goldman, I. B. Spielman, G. Juzeliūnas, and M. Lewenstein, Physical review letters **112**, 043001 (2014), https://doi.org/10.1103/PhysRevLett.112.043001.

[3] M. Mancini, G. Pagano, G. Cappellini, L. Livi, M. Rider, J. Catani, C. Sias, P. Zoller, M. Inguscio, M. Dalmonte, *et al.*, Science **349**, 1510 (2015), https://doi.org/10.1126/science.aaa8736.

[4] Z. Yan, S. Wan, and Z. Wang, Scientific reports **5**, 15927 (2015), https://doi.org/10.1038/srep15927.

[5] H. M. Price, O. Zilberberg, T. Ozawa, I. Carusotto, and N. Goldman, Physical review letters **115**, 195303 (2015), https://doi.org/10.1103/PhysRevLett.115.195303.

[6] L. F. Livi, G. Cappellini, M. Diem, L. Franchi, C. Clivati, M. Frittelli, F. Levi, D. Calonico, J. Catani, M. Inguscio, *et al.*, Physical review letters **117**, 220401 (2016), https://doi.org/10.1103/PhysRevLett.117.220401.

[7] L. Yuan, Y. Shi, and S. Fan, Optics letters **41**, 741 (2016), https://doi.org/10.1364/OL.41.000741.

[8] T. Ozawa, H. M. Price, N. Goldman, O. Zilberberg, and I. Carusotto, Physical Review A **93**, 043827 (2016), https://doi.org/10.1103/PhysRevA.93.043827.

[9] Q. Lin, M. Xiao, L. Yuan, and S. Fan, Nature communications **7**, 13731 (2016), https://doi.org/10.1038/ncomms13731.

[10] K. Fang, J. Luo, A. Metelmann, M. H. Matheny, F. Marquardt, A. A. Clerk, and O. Painter, Nature Physics **13**, 465 (2017), https://doi.org/10.1038/nphys4009.

[11] H. M. Price, T. Ozawa, and N. Goldman, Physical Review A **95**, 023607 (2017), https://doi.org/10.1103/PhysRevA.95.023607.

[12] M. Lohse, C. Schweizer, H. M. Price, O. Zilberberg, and I. Bloch, Nature **553**, 55 (2018), https://doi.org/10.1038/nature25000.

[13] O. Zilberberg, S. Huang, J. Guglielmon, M. Wang, K. P. Chen, Y. E. Kraus, and M. C. Rechtsman, Nature **553**, 59 (2018), https://doi.org/10.1038/nature25011.

[14] D.-W. Wang, R.-B. Liu, S.-Y. Zhu, and M. O. Scully, Physical review letters **114**, 043602 (2015), https://doi.org/10.1103/PhysRevLett.114.043602.

[15] L. Chen, P. Wang, Z. Meng, L. Huang, H. Cai, D.-W. Wang, S.-Y. Zhu, and J. Zhang, Physical Review Letters **120**, 193601 (2018), https://doi.org/10.1103/PhysRevLett.120.193601.

[16] X.-W. Luo, X. Zhou, C.-F. Li, J.-S. Xu, G.-C. Guo, and Z.-W. Zhou, Nature communications **6**, 7704 (2015), https://doi.org/10.1038/ncomms8704.

[17] X.-F. Zhou, X.-W. Luo, S. Wang, G.-C. Guo, X. Zhou, H. Pu, and Z.-W. Zhou, Physical review letters **118**, 083603 (2017), https://doi.org/10.1103/PhysRevLett.118.083603.

[18] B. Y. Sun, X. W. Luo, M. Gong, G. C. Guo, and Z. W. Zhou, Physical Review A **96**, 013857 (2017), https://doi.org/10.1103/PhysRevA.96.013857.

[19] Z.-D. Cheng, Z.-D. Liu, X.-W. Luo, Z.-W. Zhou, J. Wang, Q. Li, Y.-T. Wang, J.-S. Tang, J.-S. Xu, C.-F. Li, *et al.*, Optics letters **42**, 2042 (2017), https://doi.org/10.1364/OL.42.002042.

[20] X.-W. Luo, X. Zhou, J.-S. Xu, C.-F. Li, G.-C. Guo, C. Zhang, and Z.-W. Zhou, Nature communications **8**, 16097 (2017), https://doi.org/10.1038/ncomms16097.

[21] Z.-D. Cheng, Q. Li, Z.-H. Liu, F.-F. Yan, S. Yu, J.-S. Tang, Z.-W. Zhou, J.-S. Xu, C.-F. Li, and G.-C. Guo, Applied Physics Letters **112**, 201104 (2018), https://doi.org/10.1063/1.5025132.

[22] X.-W. Luo, C. Zhang, G.-C. Guo, and Z.-W. Zhou, Physical Review A **97**, 043841 (2018), https://doi.org/10.1103/PhysRevA.97.043841.

[23] L. Yuan, M. Xiao, Q. Lin, and S. Fan, Physical Review B **97**, 104105 (2018), https://doi.org/10.1103/PhysRevB.97.104105.

[24] F. D. M. Haldane, Phys. Rev. Lett. **61**, 2015 (Oct 1988), https://link.aps.org/doi/10.1103/PhysRevLett.61.2015.

[25] J. Leach, M. J. Padgett, S. M. Barnett, S. Franke-Arnold, and J. Courtial, Phys. Rev. Lett. **88**, 257901 (Jun 2002), https://doi.org/10.1103/PhysRevLett.88.257901.

[26] M. Born and E. Wolf, *Principles of optics: electromagnetic theory of propagation, interference and diffraction of light* (Elsevier, 2013).

[27] X.-L. Qi, T. L. Hughes, and S.-C. Zhang, Phys. Rev. B **78**, 195424 (Nov 2008), https://link.aps.org/doi/10.1103/PhysRevB.78.195424.

[28] T. Fukui, Y. Hatsugai, and H. Suzuki, Journal of the Physical Society of Japan **74**, 1674 (2005), https://doi.org/10.1143/JPSJ.74.1674.

[29] M. Hafezi, E. A. Demler, M. D. Lukin, and J. M. Taylor, Nature Physics **7**, 907 (2011).

[30] D. F. Walls and G. J. Milburn, *Quantum optics* (Springer Science & Business Media, 2007) https://doi.org/10.1007/978-3-540-28574-8.

[31] H. T. Lam, Y. Yu, and K. Y. Szeto, Phys. Rev. A **93**, 052319 (May 2016), https://link.aps.org/doi/10.1103/PhysRevA.93.052319.

[32] L. Lu, L. Fu, J. D. Joannopoulos, and M. Soljačić, Nature photonics **7**, 294 (2013), https://doi.org/10.1038/nphoton.2013.42.